Journal of
Materials Chemistry A

Materials for energy and sustainability

rsc.li/materials-a

ROYAL SOCIETY
OF CHEMISTRY
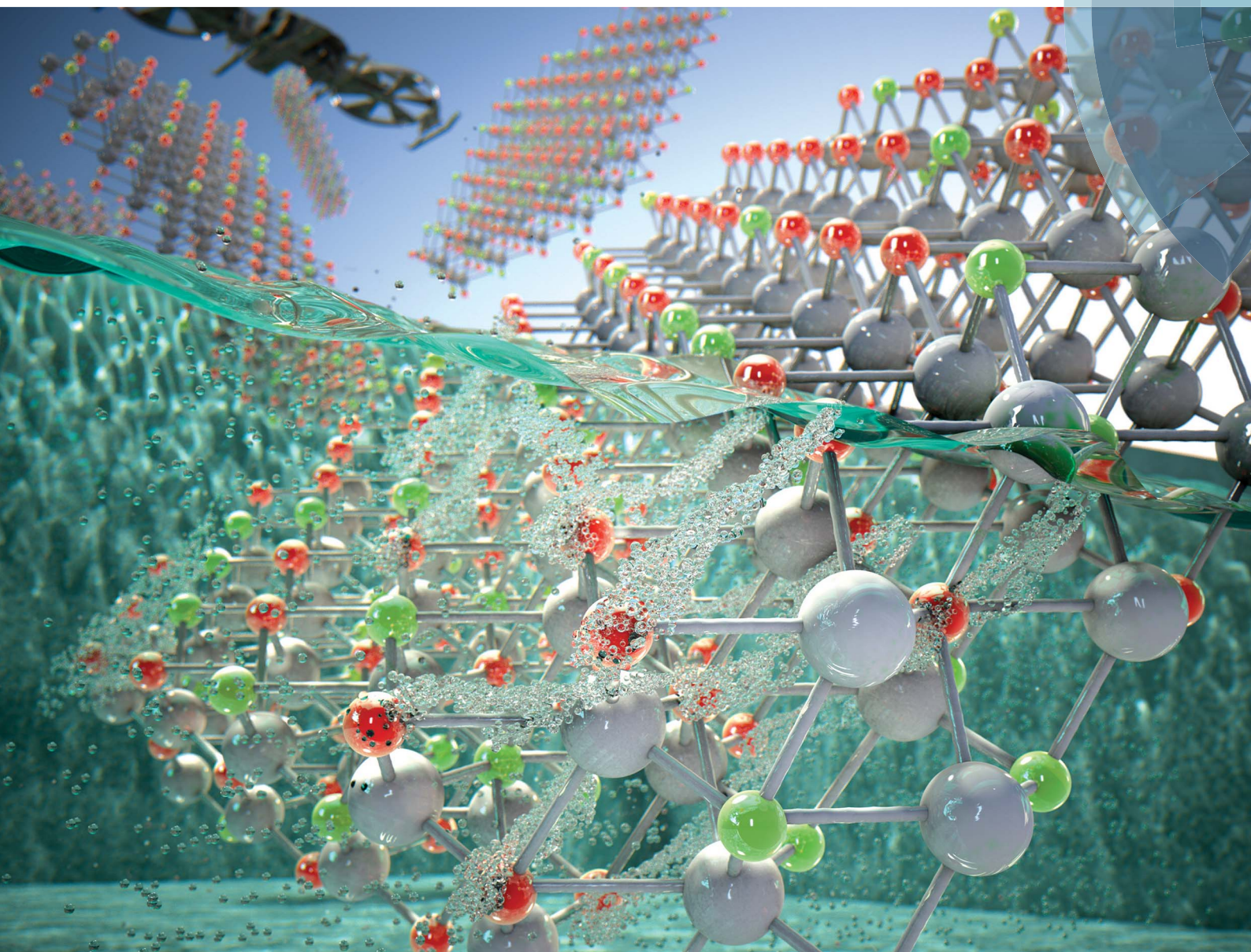
PAPER
Soo Young Kim, Ho Won Jang *et al.*
Drastically enhanced hydrogen evolution activity by 2D to 3D structural transition in anion-engineered molybdenum disulfide thin films for efficient Si-based water splitting photocathodes

PAPER

Check for updates

Drastically enhanced hydrogen evolution activity by 2D to 3D structural transition in anion-engineered molybdenum disulfide thin films for efficient Si-based water splitting photocathodes†

Ki Chang Kwon,‡[ab] Seokhoon Choi,‡[a] Joohee Lee,[b] Kootak Hong,[a] Woonbae Sohn,[a] Dinsefa Mensur Andoshe,[a] Kyoung Soon Choi, [c] Younghye Kim,[a] Seungwu Han,[a] Soo Young Kim *[b] and Ho Won Jang *[a]

We synthesized transferrable and transparent anion-engineered molybdenum disulfide thin-film catalysts through a simple thermolysis method by using [$(NH_4)_2MoS_4$] solution and powder precursors with different sulphur/phosphorus weight ratios. The synthesized sulphur-doped molybdenum phosphide (S:MoP) thin film changed from a two-dimensional van der Waals structure to a three-dimensional hexagonal structure by introduction of phosphorus atoms in the MoS_2 thin film. The S:MoP thin film catalyst, which is composed of cheap and earth abundant elements, could provide the lowest onset potential and the highest photocurrent density for planar p-type Si photocathodes. The density functional theory calculations indicate that the surface of S:MoP thin films absorb hydrogen better than that of MoS_2 thin films. The structurally engineered thin film catalyst facilitates the easy transfer of photogenerated electrons from the p-Si light absorber to the electrolyte. Anion-engineering of the MoS_2 thin film catalyst would be an efficient way to enhance the catalytic activity for photoelectrochemical water splitting.

Introduction

The depletion of fossil fuels has raised a global concern regarding the energy crisis and environment. In recent years, hydrogen fuels have been widely investigated as sustainable and renewable alternatives to fossil fuels.[1–3] Most of the hydrogen is produced by steam reforming which generates carbon dioxide and consumes a large amount of electricity.[4–6] At present, hydrogen production through photoelectrochemical (PEC) water-splitting is being extensively studied as a potential sustainable fuel production method to meet the increasing energy demands. In the pursuit of developing efficient and durable photoelectrodes, p-type silicon (p-Si) has been widely studied as it is considered as one of the most promising candidates for photocathodes for the hydrogen evolution reaction (HER) because of its absorption of wide ranges of the solar spectrum, earth abundance (low cost), and well-organized production technologies.[7–10]

However, the surface of p-Si has poor kinetics for absorbing protons (H^+) because of its high hydrogen adsorption Gibbs free energy (ΔG_H). This increases the overpotential between the surface of p-Si and electrolyte.[8,9] In addition to this overpotential issue, Si is thermodynamically vulnerable to photoactive dissolution or photocorrosion. To resolve the poor kinetics of p-Si surfaces, noble metals such as Pt, Ir, and Rh are widely used as HER catalysts.[11–13] Even though these catalysts are suitable for water splitting at low overpotentials, the scarcity, high cost, and maintenance of the high current density of these materials are significant challenges in developing alternative energy systems. Furthermore, nanoparticle-shaped noble metal catalysts cannot prevent the photoactive dissolution of p-Si photocathodes.[14–16] As a consequence, the development of highly efficient earth abundant element-based photocatalysts has become imperative for replacing noble metal-based photocatalysts.

aDepartment of Materials Science and Engineering, Research Institute of Advanced Materials, Seoul National University, Seoul 08826, Republic of Korea. E-mail: hwjang@snu.ac.kr

bSchool of Chemical Engineering and Materials Science, Chung-Ang University, Seoul 06974, Republic of Korea. E-mail: sooyoungkim@cau.ac.kr

cAdvanced Nano Surface Research Group, Korea Basic Science Institute, Daejeon 34133, Republic of Korea

† Electronic supplementary information (ESI) available: Absorbance spectra, transmittance, *I–V* sweep measurements (Fig. S1), XPS analysis (Fig. S2 and S3), AFM images for the synthesized thin films (Fig. S4 and S5), TEM images of the synthesized thin films (Fig. S7 and S8), electrochemical performance of the synthesized thin films (Fig. S9), cyclic voltammetric curves and statistical data (Fig. S10), incident-photon-to-current conversion efficiency (IPCE) measurements (Fig. S11) and flat band and band bending diagrams (Fig. S12) are available. See DOI: 10.1039/c7ta03845c

‡ These authors contributed equally to this work.

Two-dimensional transition metal disulfides (2D TMDs) such as MoS_2 and WS_2 are regarded as promising candidates to replace noble metal catalysts because TMD nanostructures inherently have large surface-to-volume ratios and possess high densities of catalytically active edge sites for the HER.[17–21] It has been reported that the edge sites of MoS_2 could be more catalytically active than its basal plane.[22] In our previous study, MoS_2 thin film catalysts with c-domains of vertically stacked region exhibited excellent HER performances.[23] However, MoS_2 thin films mainly consist of a 2D layered structure, in which each layer is weakly bound to the adjacent layers by van der Waals forces. Although thick MoS_2 films exhibit good HER performance because of the presence of many active sites, their adhesion on p-Si photocathodes is poor owing to their weak van der Waals forces. Such a poor adhesion between MoS_2 layers and between the bottom MoS_2 layer and the p-Si substrate is not enough for the long-term stability of p-Si photocathodes. On the other hand, thin MoS_2 films adhere well onto p-Si substrates and exhibit a low catalytic activity owing to the lack of active sites.

Meanwhile, transition metal phosphides (TMPs) such as Ni_2P, CoP, MoP, and FeP also have attracted much attention as promising candidates to substitute Pt because of their high catalytic activity for the HER and good stability.[24–26] Among these previously reported TMP catalysts, molybdenum phosphide (MoP) has been extensively investigated as an HER catalyst because it is a 3D hexagonal material and is a counterpart of 2D-layered MoS_2. Owing to their crystal structure, the inherent dangling bonds on the surface of thick MoP films facilitate their adhesion to p-Si substrates, indicating that long-term stability can be achieved even for thick MoP/p-Si heterojunction photocathodes. Furthermore, thick MoP films, which exhibit low ΔG_H as compared to MoS_2 basal plane and have many dangling bonds on their surface, have been reported to be good "H delivery" materials.[27] MoP catalysts have been successfully synthesized by various methods. Deng et al. synthesized 3D MoP sponges by sintering of ammonium molybdate tetrahydrate and ammonium hydrogen phosphate.[28] 3D MoP can act as both an electrode and a catalyst. Ye et al. synthesized a $MoS_{2(1-X)}P_X$ solid solution by mixing MoS_2 and red phosphorus powders.[27] An increase in the surface area of $MoS_{2(1-X)}P_X$ solid solution led to an improvement in its HER activity. Even though 2D TMD and TMP nanoparticles show electrochemical HER catalytic activities, the photocorrosion of p-Si PEC catalysis cannot be prevented. Furthermore, to the best of our knowledge, the catalytic activity of phosphorus-doped MoS_2 (P:MoS_2) and sulfur-doped molybdenum phosphide (S:MoP)-based thin film catalysts for the photoelectrochemical HER has not been reported yet.

Here, we demonstrate the wafer-scale fabrication of S:MoP/p-Si heterojunctions by using a thin-film transfer method for highly efficient photoelectrochemical hydrogen production. By controlling the S/P powder precursor ratios, P:MoS_2 and S:MoP thin films were synthesized by simple thermolysis of an ammonium tetrathiomolybdate [(NH$_4$)$_2$MoS$_4$] solution precursor on SiO$_2$/Si substrates. The P:MoS_2 and S:MoP thin film layers were transferred to a p-Si photocathode (see the

Experimental section for details). The synthesized thin films with different S/P ratios gradually transformed from 2D-layered MoS_2 (S) to P:MoS_2 (S-rich, S/P = 3, S/P = 1) and 3D hexagonal S:MoP (P-rich, S/P = 0.33, P). At an S/P ratio of 0.33, the photocurrent density at 0 V reached the peak value of 33.13 mA cm^{-2}. At a photocurrent (J_{ph}) of 1 mA cm^{-2}, the onset potential of the film shifted by 0.65 V with respect to that of a bare p-Si photocathode. This is one of the highest overpotential reduction value reported till date for HER catalysts without noble metals. The energy band diagram clearly showed that metallic S:MoP thin film catalysts can efficiently transport the photogenerated electrons from p-Si to the electrolyte interfaces. The density-functional-theory (DFT) calculations also revealed that thermo-neutral hydrogen adsorption on the S:MoP surface may account for the efficient HER.

Experimental section

DFT calculations

We carried out the density functional theory (DFT) calculations using the Vienna Ab initio Simulation Package (VASP) code based on the projector augmented wave (PAW) pseudopotential.[29,30] The cutoff energy for the plane-wave basis set was chosen to be 400 eV, and we used k-space meshes of $4 \times 4 \times 1$ for the MoPS and MoS_2 basal plane, and $2 \times 1 \times 1$ for the MoS_2 edge for the supercells in Fig. 1. The ionic configurations were relaxed until the atomic forces are reduced to within 0.02 eV Å^{-1}. The zero-point energy of the H atom was included, and the entropy of H$_2$ gas was obtained from a thermodynamic table.

MoS$_2$, P:MoS$_2$, and S:MoP thin film synthesis

SiO$_2$ (300 nm)/Si wafers were cleaned with a standard piranha solution (3 : 1 mixture of H$_2$SO$_4$ and H$_2$O$_2$) by conventional cleaning procedures followed by ultrasonication in acetone, isopropyl alcohol, and deionized (DI) water. To obtain hydrophilic surfaces on the SiO$_2$/Si wafers, O$_2$ plasma and UV-O$_3$ surface treatments were sequentially performed for 15 min, respectively. The precursor solution was prepared by dissolving (NH$_4$)$_2$MoS$_4$ powder (Sigma-Aldrich, 99.97% purity) in ethylene
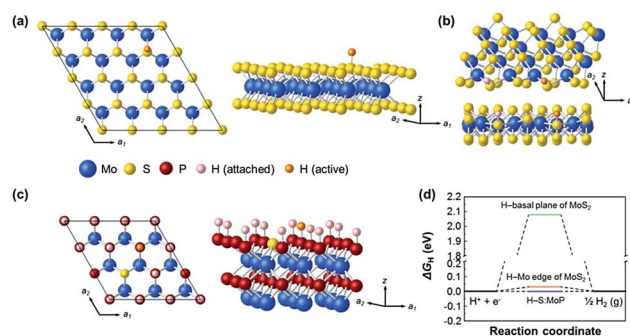

Fig. 1 Hydrogen adsorption energies obtained from the DFT calculation. (a) Basal plane of MoS$_2$, assuming $\theta = \sim 0$. (b) (10$\bar{1}$0) Mo-edge, H coverage $\theta = 0.5$. (c) S:MoP surface, $\theta = 0.875$. (d) Free energy diagram of H adsorption on the edge sites, (i) basal plane of MoS$_2$, (ii) Mo-edge of MoS$_2$, and (iii) surface of S:MoP.

This journal is © The Royal Society of Chemistry 2017

J. Mater. Chem. A, 2017, 5, 15534–15542 | 15535

glycol (Sigma-Aldrich, 99.8% purity, anhydrous) at a concentration of 500 mM. The precursor solution was spin-coated onto the prepared SiO$_2$/Si substrate at 3500 rpm for 60 s. High-purity H$_2$ and N$_2$ gases were used for the thermolysis process in a thermal chemical vapor deposition (CVD) system. First, the CVD chamber temperature was increased to 500 °C and was maintained at this temperature for 30 min under the flow of H$_2$ and N$_2$ at 1 Torr. The flow rate of H$_2$ and N$_2$ was set at 40 and 200 cm^3 min^{-1}, respectively, by using mass flow controllers. The thermolysis process was started slowly under a H$_2$ gas atmosphere and at a relatively high temperature. Then, the temperature of the CVD furnace was increased to 950 °C and was maintained for 1 h. The sublimation of powder precursors, which have particular weight ratios (S, S/P = 3, S/P = 1, S/P = 0.33, P) of sulfur to phosphorus powder (S: Sigma-Aldrich, 99.5% purity, P: Sigma-Aldrich, 99.9%), was initiated in the other heating zone, whose temperature was set at 400 °C. Once the thermolysis was complete, PMMA was spin-coated onto the CVD-grown thin films. The edges of the synthesized thin films were scratched by using a razor blade to promote the rapid separation of the synthesized thin films from the SiO$_2$/Si substrate. The PMMA/thin films/SiO$_2$/Si substrate was immersed in a buffered oxide etch (BOE, Sigma-Aldrich, 40%) to separate the thin films from the substrate by etching away the SiO$_2$ layers. The obtained thin films were washed with deionized water seven to nine times to remove the residual etchants and were transferred to an arbitrary substrate (glass, SiO$_2$, gold, or p-Si substrates). After the PMMA/thin film membranes had perfectly adhered to the substrates, the PMMA layers were removed using acetone and toluene at 50 °C for 1 h.

Materials characterization

The Raman spectra of the synthesized thin films were recorded with a Lab RAM HR (Horiba JobinYvon, Japan) at an excitation wavelength of 532 nm. The non-contact-mode AFM (XE-100, Park Systems) measurements at a scanning rate of 0.5 Hz were performed to examine the surface morphology and to determine the thickness of the synthesized MoS$_2$ thin films. Synchrotron radiation photoelectron spectroscopy experiments were carried out in an ultra-high vacuum chamber (base pressure of *ca.* 10^{-10} Torr) with a 4D beam line, equipped with an electron analyzer and a heating element at the Pohang Acceleration Laboratory. The onset of photoemission corresponding to the vacuum level at the surface of the MoS$_2$ thin films was measured by applying an incident photon energy of 350 eV with a negative bias on the sample. The results were corrected for the charging effects using Au 4f as an internal reference. The bright-field and high-resolution TEM (JEOL JEM-2100F, 200 kV) images were obtained to investigate the microstructure of the synthesized thin films. The absorption spectra of the synthesized thin films were measured by UV-Visible spectroscopy (JASCO-670).

PEC characterization

The HER measurements (Ivium Technologies, Model: Nstat) were carried out with a three-electrode system using a saturated calomel electrode as the reference electrode and a graphite rod as the counter electrode in a 0.5 M H$_2$SO$_4$ standard electrolyte solution. The three-electrode system was set up inside a quartz vessel, which protected the samples from UV absorption. A Xe arc lamp was used and calibrated to an output of 100 mW cm^{-2} (AM 1.5 G condition). For measuring the stability of each photocathode (*i.e.*, bare p-Si, MoS$_2$ (S)/p-Si, and S:MoP (S/P = 0.33)/p-Si), we used a graphite rod counter electrode (WonATech Co., Ltd) to avoid the deposition of Pt on the working electrode. A scan rate of 10 mV s^{-1} was used for the linear sweep. The incident-photon-to-current conversion efficiency was measured with a light source and a monochromator. The quantum efficiency was measured with a standard Si photodiode. EIS was conducted by applying a constant potential of 0.27 V *vs.* the RHE near the open-circuit potential. The sweeping frequency was varied from 250 kHz to 1 Hz using a 10 mV AC dither. The faradaic efficiency was calculated by using a gas chromatography measurement system (FID-GC, PerkinElmer, NARL8502 Model 4003).

Results and discussion

The hydrogen-evolution activity of a PEC catalyst strongly correlates with the energy required for chemisorption of atomic hydrogen at the catalytic site or the Gibbs free energy for the hydrogen binding (ΔG_H).[31,32] To evaluate the catalytic activity of S:MoP for the HER, we conducted DFT calculations and obtained ΔG_H on the surface of S:MoP thin films using the following relationship:

$$\Delta G_H = \Delta E_H + \Delta E_{ZPE} - T\Delta S \qquad (1)$$

where ΔE_H is the internal energy of hydrogen adsorption, ΔE_{ZPE} is the zero-point energy, T is the temperature, and ΔS is the entropy change. ΔE_H is computed as follows:

$$\Delta E_H = E(*nH) - E(*(n-1)H) - 1/2E(H_2) \qquad (2)$$

where $E(H_2)$ is the total energy of a hydrogen molecule and $E(*nH)$ is the energy when n hydrogen atoms are bound at active sites. This means that ΔE_H depends on the H coverage (θ). When the hydrogen binding energy at a certain θ is negative, the equilibrium value of H coverage can be estimated from the adsorption isotherm as the upper value of the coverage.[33] That is to say, we assumed that the relevant H binding energy is at the average H coverage. The θ values for the MoS$_2$ basal plane, MoS$_2$ edge, and S:MoP surface were ~0, 0.5, and 0.875, respectively in the present models. The main results are shown in Fig. 1. For comparison, we also calculated ΔG_H on the basal plane and edge of the MoS$_2$ system. According to the Sabatier's principle, a near-zero value of hydrogen binding energy is optimal for PEC catalysts so that H can be readily attached to and detached from the catalyst surface to facilitate the reaction. From the computational results shown in Fig. 1(d), it is seen that S:MoP is more active than MoS$_2$ edges that are known to be active for the HER, as well as the inert basal plane of MoS$_2$. The ΔG_H value (~0.05 eV) of the S:MoP thin film was much lower than that reported

15536 | *J. Mater. Chem. A*, 2017, 5, 15534–15542

This journal is © The Royal Society of Chemistry 2017

for $MoS_{(1−X)}P_X$ solid solution catalysts ($\sim$0.7 eV), in which a P atom is substituted into the MoS_2 lattice structure.[27] This marked change in ΔG_H can be attributed to the presence of many dangling bonds on the surface of S:MoP thin films. Our results clearly show that the 3D hexagonal P-rich S:MoP thin film could act as an efficient HER catalyst.

The P:MoS_2 and S:MoP thin films used in this study were synthesized by simple thermolysis of an ethylene glycol solution of [$(NH_4)_2MoS_4$]. To elucidate the role of phosphorus substitution on the catalytic activity of the MoS_2 thin film catalyst, a 500 mM [$(NH_4)_2MoS_4$] solution, which showed a moderate catalytic activity in our previous study, was used as the base precursor.[23] The schematic of the thermolysis method used in this study is shown in Fig. 2(a). The 500 mM [$(NH_4)_2MoS_4$] solution was spin-coated onto a SiO_2/Si substrate. By changing the S/P powder precursor ratio, the MoS_2 (S), P:MoS_2 (S-rich, S/P = 3 and S/P = 1), and S:MoP (P-rich, S/P = 0.33 and P) thin films were successfully synthesized. MoS_2 and MoP exhibit a hexagonal atomic structure ($P6_3/mmc$) in which a Mo atom is coordinated with six S and P atoms as displayed in Fig. 2(b). Since the lattice structures of MoS_2 and MoP are similar to each other,[34] the substitutional dopant P atoms could replace the S atoms in the [$(NH_4)_2MoS_4$] precursor layer during the growth step. Furthermore, the atomic radii of S and P are almost the same. Hence, P atoms can act as anions in hexagonal MoX_2 (X = S and P) without breaking its structure. The MoS_2 surface is free of dangling bonds, while some inherent dangling bonds exist at the surface of MoP. Since dangling bonds are electrochemical active sites, MoP can act as an efficient HER catalyst. For the characterization of the synthesized thin films and their application as PEC catalysts, they had to be transferred to a substrate. Glass, p-Si, and SiO_2/Si are widely used as substrates for such films. Poly[methyl methacrylate] (PMMA) was used as the supporting polymer and was spin-coated onto the synthesized thin films for wet transfer. The PMMA/thin films were separated from the SiO_2/Si substrates by immersing them in a bath of hydrogen fluoride and a buffered oxide etchant. Then, the separated films were transferred onto arbitrary substrates. The photographic images of the synthesized thin films transferred on glass substrates are shown in Fig. 2(c). The color of the synthesized MoS_2 thin film, which was greenish-yellow, gradually turned black with an increase in the amount of phosphorus powder. The transmittance of anion-engineered MoS_2 thin films was gradually increased with respect to the increase of P amounts (see Fig. S1, ESI†). The absorbance and the current–voltage (I–V) sweep curve data clearly show that anion-engineered MoS_2 thin films were drastically changed to the metallic S:MoP from the semiconducting MoS_2 (see Fig. S1, ESI†). Furthermore, the photographic images of the PMMA/S:MoP layer suspended in deionized water and a 6 cm × 6 cm S:MoP thin film suspended on a four-inch p-Si wafer are shown in Fig. 2(c).

Raman spectroscopy is a powerful tool to detect the atomic vibrations in thin films, especially 2D layered materials. For a MoS_2 layer, the in-plane vibration appears near 384 cm^{-1}, while the out-of-plane vibration appears near 410 cm^{-1}.[35] The Raman spectra of the MoS_2, P:MoS_2, and S:MoP thin films synthesized with different S/P powder precursor ratios are shown in Fig. 3(a). Two characteristic peaks, E^1_{2g} (in-plane vibration) and A_{1g} (out-of-plane vibration), appeared around
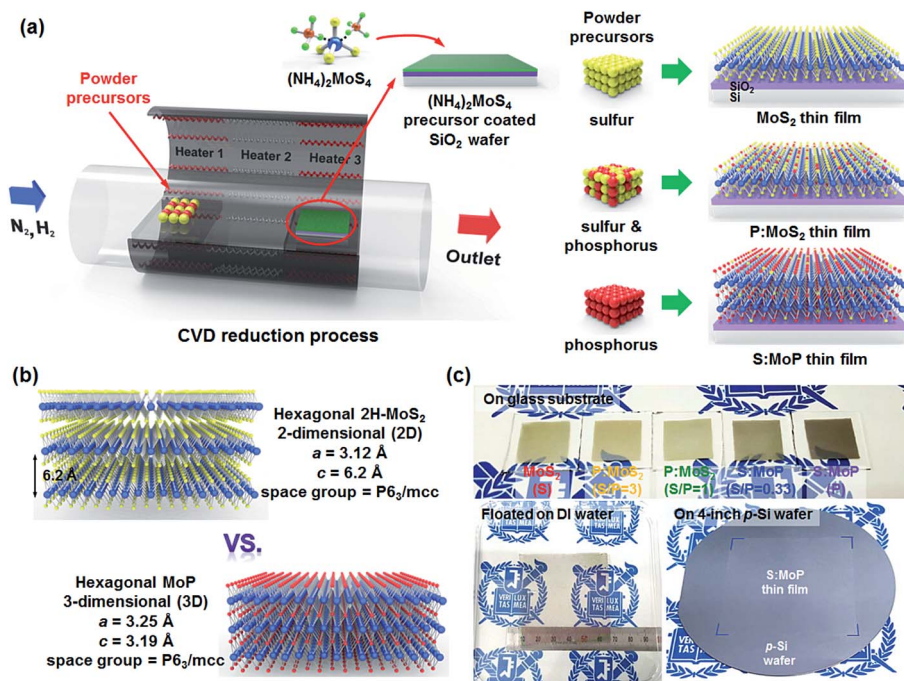

Fig. 2 Schematic of experimental procedures and photographic images of large-area synthesis of sulfur-doped molybdenum phosphide. (a) The synthetic procedure for sulphur-doped MoP thin film catalysts. (b) Atomic structures of MoS_2 and MoP. (c) Photographic images of the thin films transferred onto the glass substrate, floated onto a deionized water bath, and transferred onto a four-inch p-Si wafer.
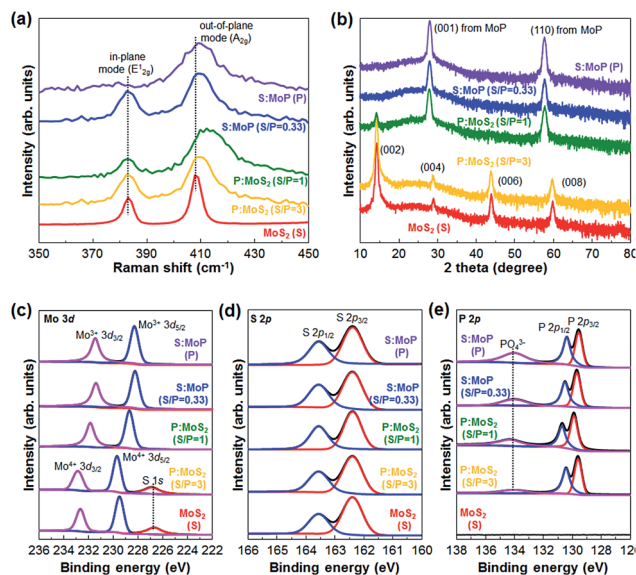
Fig. 3 Characterization of the synthesized thin films grown by a simple thermolysis method with various S/P ratios. (a) Raman spectra of the synthesized thin films. The E_{2g}^1 peaks significantly reduced when the MoS_2 layer was doped with phosphorus. (b) XRD spectra of the synthesized thin films. The MoS_2 peaks disappeared at S : P = 1 : 1. XPS core level spectra of (c) Mo 3d, (d) S 2p, and (e) P 2p of the synthesized thin films.

384 and 408 cm^{-1}, respectively. The frequency difference between these two Raman modes of MoS_2 thin films depends upon the number of layers and can be easily used as a thickness indicator.[35] The frequency difference between the E_{2g}^1 and A_{1g} modes was approximately 24 cm^{-1}, indicating that the synthesized MoS_2 thin film had multilayers. With the incorporation of phosphorus into MoS_2, the A_{1g} peak slightly shifted to a higher wavenumber as a result of the softening of the A_{1g} vibrations. Furthermore, the full width at half maximum of the A_{1g} peak showed broadening in the range of 5.1–12.3 cm^{-1}. On the other hand, the E_{2g} peak disappeared when the concentration of phosphorus atoms was much larger than that of sulphur atoms in the S:MoP thin films. These observations are analogous to the results obtained in previous studies focusing on the surface charge transfer doping of MoS_2 and electrostatic doping of MoS_2 by a back-gate potential.[36,37] Fig. 3(b) shows the X-ray diffraction (XRD) patterns of MoS_2, P:MoS_2, and S:MoP. The XRD patterns of the thin films with S and an S/P ratio of 3 show the characteristic peaks of MoS_2. When the concentration of P was comparable to or higher than that of S, the intensity of the MoS_2 peak decreased significantly and MoP peaks were observed, confirming the formation of simple hexagonal MoP thin films.[28,38] The chemical components and atomic ratios of the synthesized thin films were investigated using X-ray photoemission spectroscopy (XPS, see Fig. S2, ESI†). The core level spectra of Mo 3d, S 2p, and P 2p were recorded (Fig. 3(c)–(e)). In the Mo 3d core level spectra, the Mo^{4+} 3d$_{3/2}$ and Mo^{4+} 3d$_{5/2}$ peaks slightly shifted to lower binding energies corresponding to the Mo^{3+} 3d$_{3/2}$ and Mo^{3+} 3d$_{5/2}$ peaks, confirming the successful transformation of MoS_2 into MoP structures.

Furthermore, the peak intensity of S 1s in the Mo 3d core level spectra reduced significantly. The S 2p and P 2p core level spectra of each synthesized thin film were almost the same. Because the starting material *i.e.*, $[NH_4]_2MoS_4$ contained S atoms, the S:MoP (P) thin film showed an S 2p peak. In the P 2p core level spectra, two types of peaks were observed: two sharp peaks near ~129 eV and a broad peak near ~134 eV. The broad peak near ~134 eV corresponds to PO_4^{3-} and is a characteristic peak for MoP exposed to air.[27] The intensity of the PO_4^{3-} peak gradually increased with an increase in the weight ratio of P. The atomic ratio of Mo to S was constant at 33.2% to 67.8%. This is consistent with previous reports (see Fig. S3, ESI†).[34] The atomic ratio of P in the MoS_2 thin films increased gradually with the introduction of P into them. Furthermore, the atomic ratio of P became higher than that of S at S/P = 0.33, indicating that the synthesized thin film with only P powder precursor was a P-rich S-doped MoP thin film. Based on these measurements, the P-doped MoS_2 and S-doped MoP thin films were successfully synthesized by the thermolysis of the $[(NH_4)_2MoS_4]$ solution precursor and mixed power precursors with different S/P ratios.

To evaluate the thickness and surface morphology of the synthesized films, atomic force microscopy (AFM) was used. All the synthesized thin films were nano-granular (see Fig. S4, ESI†). The serrated surface of the synthesized films with different powder precursors provided a larger surface area than the atomically flat surface of a single-crystalline MoS_2 layer. The root-mean-square (RMS) roughness was 3 nm for the MoS_2 thin film. The RMS roughness increased from 3 to 7 nm when the MoS_2 and MoP structures coexisted in the P:MoS_2 thin films, as shown in Fig. 4(a)–(c). However, it drastically decreased from 7 nm for the P:MoS_2 thin films to 2 nm for the S:MoP thin films when P atoms were predominant in the synthesized film. Furthermore, the thickness of the synthesized films decreased significantly from 20 nm for MoS_2 to 13 nm for S:MoP (see Fig. S5, ESI†). The surface analysis of the synthesized MoS_2 and
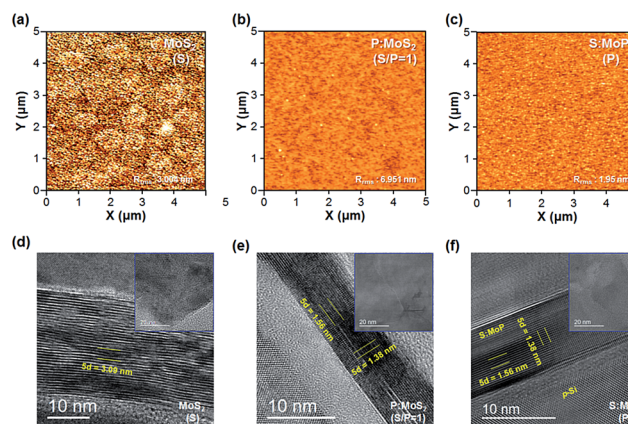

Fig. 4 Characterization of the MoS_2, P:MoS_2 (sulfur-rich), and S:MoP (phosphorus-rich) thin films. Topographic AFM images of the synthesized thin films: (a) MoS_2 (S), (b) P:MoS_2 (S/P = 1), and (c) S:MoP (P) on the SiO_2 substrate. Cross-sectional TEM images of the synthesized thin films: (d) MoS_2 (S), (e) P:MoS_2 (S/P = 1), and (f) S:MoP (P) on p-Si wafer. The inset of each figure shows the high-resolution TEM images of the thin films on the Cu grid.

S:MoP (S/P = 0.33) with 5 different regions shows the reliability of our AFM measurement (see Fig. S6, ESI†). The 20 × 20 μm^2 AFM images and the RMS roughness values clearly show that the thermolysis of solution precursor is an effective way for synthesis of the MoS$_2$ and S:MoP catalysts. MoS$_2$ is a 2D material whose layers are bound to each other by van der Waals force (*d*-spacing = 0.618 nm), while MoP is a 3D material without van der Waals forces (*d*-spacing = 0.312 nm). This resulted in a decrease in the thicknesses of the P:MoS$_2$ and S:MoP thin films. The microstructures of the synthesized thin films were studied by transmission electron microscopy (TEM). The low magnification TEM images (see Fig. S7 and S8, ESI†) show the pinhole-free thin films on a Cu grid. The synthesized films showed the 3D to 2D structural transition after the introduction of P atoms into the MoS$_2$ structure. The selected area electron diffraction pattern (SAED) of each thin film clearly showed that the atomic structure significantly changed from MoS$_2$ to MoP. The top- and cross-sectional-view high-resolution TEM images of the thin films are shown in Fig. 4(d)–(f). The thin films containing only P (S:MoP) showed a nano-granular surface. Furthermore, the *d*-spacing of the thin film containing only S (MoS$_2$ (S)) was comparable to that of the films with S/P = 1 and S:MoP (P:MoS$_2$ (S/P = 1 : 1) and S:MoP (P)). The *d*-spacing of the P:MoS$_2$ and S:MoP thin films (*d* = 0.312 nm) is consistent with that of MoP, indicating that P atoms were successfully substituted into the MoS$_2$ atomic structure by simple thermolysis.

We have investigated the electrochemical (EC) HER performance of the thin films synthesized with different S/P powder precursor ratios on an Au substrate with *iR*-correction (see Fig. S9, ESI†). The HER performance of the S:MoP (S/P = 0.33) thin films is comparable to that of the previously reported MoP catalysts.[28,38–40] The EC performance of the thin films synthesized on an Au electrode is summarized (see Table S1, ESI†). The reaction mechanism of the HER can be explained by Tafel slopes. The HER proceeds *via* a three-step mechanism involving a discharge step (Volmer reaction, Tafel slope of 120 mV dec^{-1}), a desorption step (Heyrovsky reaction, Tafel slope of 40 mV dec^{-1}), and a recombination step (Tafel reaction, 30 mV dec^{-1}).[41] In the EC measurements, the S:MoP (S/P = 0.33)/Au electrode showed a Tafel slope of 67.34 mV dec^{-1}, indicating that the HER in this case, proceeded probably with the Volmer–Heyrovsky reaction. Furthermore, this value of Tafel slope (67.34 mV dec^{-1}) indicates that the electrode had an outstanding catalytic activity, considering that our S:MoP catalysts were flat thin films with a much lower surface area than nanoparticles or nanostructures. In order to compare the HER performance of the S:MoP (S/P = 0.33)/p-Si or Au electrode with that of previously reported state-of-the-art electrodes with similar material systems, their overpotentials at 10 mA cm^{-2} and Tafel slope values are summarized (see Table S2, ESI†).

The PEC characterization of the S:MoP/p-Si photocathodes was carried out with a standard three-electrode configuration using a 0.5 M H$_2$SO$_4$ solution as the electrolyte. All the measurements were conducted with a graphite rod counter electrode. Fig. 5(a) shows the current density *vs.* potential (*J–V*) behavior of the S:MoP/p-Si photocathodes under a simulated air
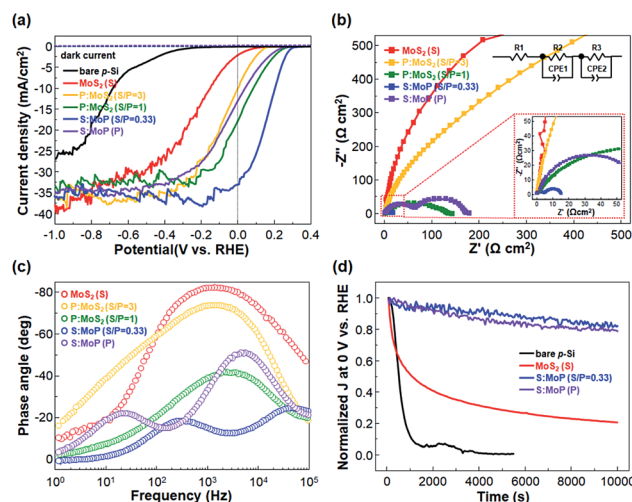

Fig. 5 Photoelectrochemical performance of the synthesized thin films/p-Si heterojunction photocathodes. (a) Linear sweep voltammetry curves of each thin film catalyst. The S:MoP (S/P = 0.33)/p-Si photocathode showed a current density of 33.13 mA cm^{-2} at 0 V and a significant potential value shift at 10 mA cm^{-2} from −0.69 to 0.082 V for p-Si. (b) Electrochemical impedance spectroscopy analysis of the synthesized thin film catalysts/p-Si heterojunction photocathodes. The inset graph shows the magnified 0 to 50 Ω cm^2 results for better understanding. (c) Bode plot of each thin film catalyst/p-Si heterojunction photocathode. (d) Stability tests over 10 000 s for the bare p-Si, MoS$_2$ (S), and S:MoP (S/P = 0.33 and P) thin films at 0 V.

mass 1.5 G condition. The dashed lines indicate the dark current. We define the onset potential in the *J–V* curve as the potential when the photocurrent density reaches −1 mA cm^{-2}. The bare p-Si photocathode showed a large negative onset potential of −0.35 V. Even though p-Si is a promising candidate for photocathodes because of its narrow band gap, which enables it to absorb a wide portion of the incident solar spectrum, an additional potential must be supplied to drive the HER because of the carrier concentration and kinetic overpotential issues.[9] The highest catalytic activity for the HER was exhibited by the S:MoP (S/P = 0.33) thin films. The onset potentials of the synthesized thin film catalysts/p-Si photocathodes shifted gradually to the anodic direction at S/P = 0.33. For the S:MoP (S/P = 0.33)/p-Si photocathode, the onset potential shifted towards the anodic direction by 0.63 V with respect to that of the bare p-Si. Furthermore, the photocurrent density at 0 V (*vs.* the RHE) reached a value of 33.13 mA cm^{-2}. It is notable that the value is even higher than the maximum photocurrent density (24.6 mA cm^{-2}) of thickness controlled n-MoS$_2$/p-Si heterojunction photocathodes in our previous study.[23] At S/P ratios greater than 0.33, the photocurrent onset shifted slightly to the cathodic direction. Because of the transfer of the S:MoP (S/P = 0.33) thin film, the potential required to reach the photocurrent of 10 mA cm^{-2} decreased from 0.685 (bare p-Si) to −0.21 V. The applied-bias photon-to-current efficiency (ABPE) was also calculated from the *J–V* curves shown in Fig. 5(a). The largest anodic shift of the onset potential resulted in a maximum applied-bias photon-to-current efficiency (ABPE) of 2.8% for the S:MoP (S/P = 0.33)/p-Si photocathode. This value is comparable to the

ABPE obtained with noble metal-decorated Si-based photocathodes.[39]

The incident-photon-to-current conversion efficiency spectra of the S:MoP/p-Si were recorded at an applied potential of 0 V *vs.* the RHE (see Fig. S11, ESI†). Among the tested photocathodes, the photocathode with an S:MoP (S/P = 0.33) layer exhibited the highest efficiency of around 80% in the wavelength range of 410–720 nm. The linear-sweep voltammetry curves show that the PEC properties of the S:MoP/p-Si photocathodes depended on the S/P powder precursor ratios and it was necessary to determine an optimum S/P ratio. The PEC performances of the thin films synthesized with different S/P powder precursor ratios on p-Si photocathodes are summarized in Table 1.

We also conducted electrochemical impedance spectroscopy (EIS) measurements using a simplified equivalent circuit as shown in Fig. 5(b). The simplified equivalent circuit consisted of constant phase elements (CPEs) and charge-transfer resistances (R_{ct}). The impedance spectra were recorded at a bias near the onset potential to avoid the possible complicated factors. The small semicircular arcs in the Nyquist plots reflect the lower charge transfer resistance at each interface. The semicircular arcs corresponding to the CPEs and R_{ct} decreased significantly and thus were clearly separated for the photocathodes with S:MoP (P-rich, S/P = 0.33 and P) thin film catalysts. This significant decrease in the overall impedance is attributed to the semiconductor–metal transition caused by phosphorus doping into the MoS$_2$ thin film. The R_{ct} values for the S:MoP (S/P = 0.33)/electrolyte interface ($R_{ct,3}$) showed the smallest value, which is two orders of magnitude smaller than the $R_{ct,3}$ value for the MoS$_2$ (S)/p-Si photocathode (Table 2). Additional information on EIS can be obtained by the Bode plot as displayed in Fig. 5(c). Two peaks corresponding to the two main processes taking place can be observed. The peaks in the high and low frequency regions represent the charge transfer from p-Si to the catalytic thin films and the charge transfer at the catalytic thin film/electrolyte interface, respectively.[42] For the P:MoS$_2$ thin film/p-Si photocathodes, the two peaks almost overlapped, leading to a single broad peak. Meanwhile, the S:MoP thin film/p-Si photocathodes showed two clearly separated peaks. For the S:MoP (S/P = 0.33) thin film/p-Si photocathode, the peak in the high frequency region shifted towards the highest frequency range and showed a significant decrease in the phase angle, suggesting that a low-resistance ohmic contact was formed between p-Si and S:MoP.[43] These are in agreement with the results obtained by linear sweep voltammetry in Fig. 5(a).

Table 1 The summarized photoelectrochemical performances of the synthesized thin films/p-Si heterojunction photocathodes

Photocathodes	Current density (mA cm^{-2}) @ 0 V	Overpotential (V) at 10 mA cm^{-2}
Bare p-Si	0.013	+0.685
MoS$_2$ (S)	2.051	+0.150
P:MoS$_2$ (S/P = 3)	10.192	−0.002
P:MoS$_2$ (S/P = 1)	18.014	−0.087
S:MoP (S/P = 0.33)	33.132	−0.207
S:MoP (P)	13.131	+0.040

Table 2 The charge transport resistances of the synthesized thin film/p-Si photocathodes

Photocathode	$R_{ct,1}$ (Ω cm^2) Contact/p-Si	$R_{ct,2}$ (Ω cm^2) p-Si/TF^a	$R_{ct,3}$ (Ω cm^2) TF/EL^b
Bare p-Si	1.17	4810^c	—
MoS$_2$ (S)	1.38	1305.1	1425.7
P:MoS$_2$ (S/P = 3)	3.04	2385.4	383.1
P:MoS$_2$ (S/P = 1)	5.14	108.9	17.7
S:MoP (S/P = 0.33)	2.15	10.0	6.6
S:MoP (P)	5.21	103.0	63.7

^{a} TF: Thin films. ^{b} EL: Electrolyte. ^{c} p-Si/electrolyte.

The long-term stability of the S:MoP/thin-film catalysts was evaluated by chronoamperometric measurements. These measurements were carried out to determine whether the catalysts could play the role of a passivation layer in p-Si. Fig. 5(d) shows the chronoamperometry curves of bare p-Si, MoS$_2$ (S)/p-Si, S:MoP (S/P = 0.33)/p-Si, and S:MoP (P)/p-Si for 10 000 s. The bare p-Si photocathode suffered from severe degradation, as reported by several groups.[39,44–47] On the other hand, in the case of the S:MoP (S/P = 0.33, P) thin film, the photocurrent degradation was considerably suppressed. Among all the thin film passivation layer-loaded photocathodes, the MoS$_2$ (S)/p-Si photocathode showed a rapid degradation. Since the MoS$_2$ (S) thin film (22 nm) used in this study is thicker than the MoS$_2$ thin film with the optimum thickness (13 nm) which shows the highest PEC performance in our previous study,[23] the top layers of the MoS$_2$ thin film were compiled by the weak van der Waals force compared to the bottom layers of MoS$_2$ thin films which form the heterojunction with the surface of p-Si. The P-rich S:MoP thin films (S/P = 0.33 and P) are hexagonal 3D materials with no interlayer van der Waals force. The reason behind the enhanced stability of the S:MoP thin film is 2D to 3D structural transition with the introduction of P atoms, which substituted the S atomic sites. The S:MoP (S/P = 0.33)/p-Si photocathode maintained more than 80% of its initial photocurrent during the operation time, suggesting that the S:MoP thin film (S/P = 0.33) protected the p-Si photocathode from severe photocorrosion.

The main light absorber in the S:MoP (S/P = 0.33)/p-Si heterostructure photocathodes was the p-Si substrate because of the semi-transparency of the S:MoP thin films. Thus, it is important to know whether the photogenerated electrons inside p-Si moved efficiently toward the S:MoP/electrolyte interface for triggering the HER. Ultraviolet photoemission spectroscopy (UPS) and XPS valence band spectra were used in order to explore the band-bending of the S:MoP (S/P = 0.33)/p-Si heterostructures. Fig. 6(a) shows the secondary electron emission (SEE) cutoffs of p-Si (4.65 eV), MoS$_2$ (S)/p-Si (4.5 eV), and S:MoP (S/P = 0.33)/p-Si (4.4 eV). We could determine the work functions of p-Si, MoS$_2$ (S), and S:MoP (S/P = 0.33) by comparing the SEE cutoff of each sample with the work function of the Au reference (5.1 eV). The energy differences between the Fermi level and the valence band maximum ($E_F - E_V$) could be obtained from the XPS valence-band spectra shown in Fig. 6(b).
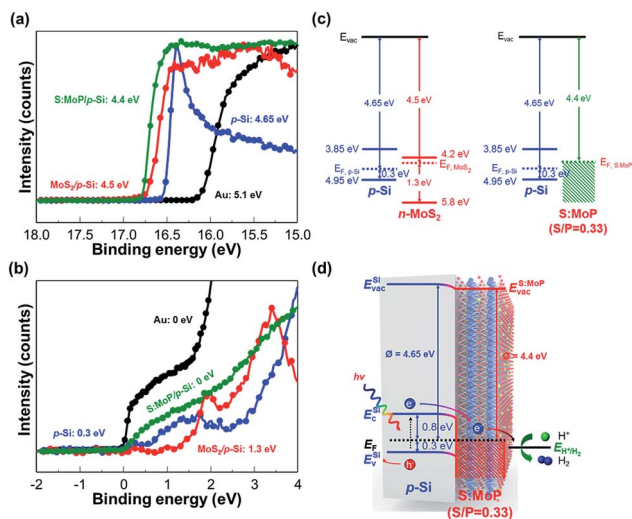
Fig. 6 Characterization of suggested energy band diagrams between p-Si and S:MoP (S/P = 0.33). (a) Ultraviolet photoemission spectroscopy (UPS) and (b) X-ray photoemission valence spectra of bare p-Si, MoS_2/p-Si, and S:MoP/p-Si. Each measured value was corrected with the Au reference. (c) Comparison of the flat band energy diagrams of MoS_2 (S) and S:MoP (S/P = 0.33) on the p-Si photocathodes. (d) Energy band diagram of the S:MoP (S/P = 0.33)/p-Si heterojunction photocathode.

The $E_F - E_V$ values for p-Si and MoS_2 (S)/p-Si were 0.3 and 1.3 eV, respectively. From the absorption spectra, the optical band gap of MoS_2 (S) was found to be around 1.6 eV, while S:MoP (S/P = 0.33) showed a zero gap (see Fig. S1, ESI†). Based on these results, the flat band and band bending diagrams for the n-MoS_2 (S)/p-Si heterostructure were obtained (see Fig. 6(c) and S12, ESI†). These diagrams were consistent with those reported in our previous study.[23] Interestingly, the $E_F - E_V$ value of the phosphorus-rich S:MoP thin film was 0 eV. The absorbance spectra revealed that the phosphorus-rich S:MoP thin film was metallic. According to the DFT calculations, the metallic S:MoP thin film with a 3D hexagonal structure is a more active catalyst compared to the 2H–MoS_2 thin film with a 2D hexagonal structure, which has a limited number of active sites for the HER. On the basis of the UPS and XPS measurement results, an energy band diagram was suggested for S:MoP (S/P = 0.33)/p-Si (Fig. 6(d)). The energy band diagram revealed that the photo-generated electrons could be easily transported to the S:MoP (S/P = 0.33)/p-Si interface and no electronic potential barrier was observed.

Conclusions

We have successfully demonstrated a simple method to improve the PEC HER catalytic activity of molybdenum disulfide thin film catalysts by introducing substitutional phosphorus dopants in their atomic structure. The S:MoP/p-Si heterojunction photocathodes showed a high photocurrent density (33.13 mA cm^{-2} at 0 V vs. the RHE), large overpotential shift (0.9 V at 10 mA cm^{-2}), and long-term stability (over 10 000 s). The characterization of the S:MoP/p-Si photocathodes

revealed that they could act not only as surface active catalysts owing to their low hydrogen adsorption Gibbs free energy but also as passivation layers owing to their 3D tight bonding between molybdenum and sulphur or phosphorus atoms. This work highlights that the anion substitution in MoS_2 thin films is an effective way to enhance the PEC performance of the thin films.

Author contributions

Acknowledgements

Notes and references

1 X. Chen, S. Shen, L. Guo and S. S. Mao, *Chem. Rev.*, 2010, **110**, 6503–6570.
2 F. E. Osterloh and B. A. Parkinson, *MRS Bull.*, 2011, **36**, 17–22.
3 A. Kudo and Y. Miseki, *Chem. Soc. Rev.*, 2009, **38**, 253–278.
4 L. B. Braga, J. L. Silveira, M. E. Da Silva, C. E. Tuna, E. B. Machin and D. T. Pedroso, *Renewable Sustainable Energy Rev.*, 2013, **28**, 166–176.
5 D. G. Nocera, *Acc. Chem. Res.*, 2012, **45**, 767–776.
6 A. Haryanto, S. Fernando, N. Murali and S. Adhikari, *Energy Fuels*, 2005, **19**, 2098–2106.
7 M. G. Walter, E. L. Warren, J. R. McKone, S. W. Boettcher, Q. Mi, E. A. Santori and N. S. Lewis, *Chem. Rev.*, 2010, **110**, 6446–6473.
8 N. C. Strandwitz, D. B. Turner-Evans, A. C. Tamboli, C. T. Chen, H. A. Atwater and N. S. Lewis, *Adv. Energy Mater.*, 2012, **2**, 1109–1116.
9 D. M. Andoshe, J.-M. Jeon, S. Y. Kim and H. W. Jang, *Electron. Mater. Lett.*, 2015, **11**, 323–335.
10 K. Osseo-Asare, D. Wei and K. K. Mishra, *J. Electrochem. Soc.*, 1996, **143**, 749–751.
11 E. L. Warren, S. W. Boettcher, J. R. McKone and N. S. Lewis, *SPIE-Int. Soc. Opt. Eng., Proc.*, 2010, **7770**, 77701F.
12 L. Zhu, H. Lin, Y. Li, F. Liao, Y. Lifshitz, M. Sheng, S.-T. Lee and M. Shao, *Nat. Commun.*, 2016, **7**, 12272.
13 M. Li, Q. Ma, W. Zi, X. Liu, X. Zhu and S. F. Liu, *Sci. Adv.*, 2015, **1**, e1400268.

This journal is © The Royal Society of Chemistry 2017

J. Mater. Chem. A, 2017, **5**, 15534–15542 | **15541**

14 J. Kye, M. Shin, B. Lim, J.-W. Jang, I. Oh and S. Hwang, *ACS Nano*, 2013, **7**, 6017–6023.

15 S. Y. Reece, J. A. Hamel, K. Sung, T. D. Jarvi, A. J. Esswein, J. J. Pijpers and D. G. Nocera, *Science*, 2011, **334**, 645–648.

16 Y. Hou, B. L. Abrams, P. C. Vesborg, M. E. Björketun, K. Herbst, L. Bech, A. M. Setti, C. D. Damsgaard, T. Pedersen, O. Hansen, J. Rossmeisl, S. Dahl, J. K. Nørskov and I. Chorkendorff, *Nat. Mater.*, 2011, **10**, 434–438.

17 D. Voiry, H. Yamaguchi, J. Li, R. Silva, D. C. Alves, T. Fujita, M. Chen, T. Asefa, V. B. Shenoy, G. Eda and M. Chhowalla, *Nat. Mater.*, 2013, **12**, 850–855.

18 K. C. Kwon, C. Kim, Q. V. Le, S. Gim, J.-M. Jeon, J. Y. Ham, J.-L. Lee, H. W. Jang and S. Y. Kim, *ACS Nano*, 2015, **9**, 4146–4155.

19 A. B. Laursen, S. Kegnæs, S. Dahl and I. Chorkendorff, *Energy Environ. Sci.*, 2012, **5**, 5577–5591.

20 H. Li, C. Tsai, A. L. Koh, L. Cai, A. W. Contryman, A. H. Fragapane, J. Zhao, H. S. Han, H. C. Manoharan, F. Abild-Pedersen, J. K. Nørskov and X. Zheng, *Nat. Mater.*, 2016, **15**, 48–53.

21 T. F. Jaramillo, K. P. Jørgensen, J. Bonde, J. H. Nielsen, S. Horch and I. Chorkendorff, *Science*, 2007, **317**, 100–102.

22 D. Voiry, M. Salehi, R. Silva, T. Fujita, M. Chen, T. Asefa, V. B. Shenoy, G. Eda and M. Chhowalla, *Nano Lett.*, 2013, **13**, 6222–6227.

23 K. C. Kwon, S. Choi, K. Hong, C. W. Moon, Y.-S. Shim, D. H. Kim, T. Kim, W. Sohn, J.-M. Jeon, C.-H. Lee, K. T. Nam, S. Han, S. Y. Kim and H. W. Jang, *Energy Environ. Sci.*, 2016, **9**, 2240–2248.

24 E. J. Popczun, J. R. McKone, C. G. Read, A. J. Biacchi, A. M. Wiltrout, N. S. Lewis and R. E. Schaak, *J. Am. Chem. Soc.*, 2013, **135**, 9267–9270.

25 F. H. Saadi, A. I. Carim, E. Verlage, J. C. Hemminger, N. S. Lewis and M. P. Soriaga, *J. Phys. Chem. C*, 2014, **118**, 29294–29300.

26 P. Jiang, Q. Liu, Y. Liang, J. Tian, A. M. Asiri and X. Sun, *Angew. Chem., Int. Ed.*, 2014, **53**, 12855–12859.

27 R. Ye, P. del Angel-Vicente, Y. Liu, M. J. Arellano-Jimenez, Z. Peng, T. Wang, Y. Li, B. I. Yakobson, S. H. Wei, M. J. Yacaman and J. M. Tour, *Adv. Mater.*, 2015, **28**, 1427–1432.

28 C. Deng, F. Ding, X. Li, Y. Guo, W. Ni, H. Yan, K. Sun and Y.-M. Yan, *J. Mater. Chem. A*, 2016, **4**, 59–66.

29 G. Kresse and J. Furthmüller, *Phys. Rev. B: Condens. Matter Mater. Phys.*, 1996, **54**, 11169–11186.

30 P. E. Blöchl, *Phys. Rev. B: Condens. Matter Mater. Phys.*, 1994, **50**, 17953–17979.

31 T. Bligaard, J. Nørskov, S. Dahl, J. Matthiesen, C. Christensen and J. Sehested, *J. Catal.*, 2004, **224**, 206–217.

32 M. Cabán-Acevedo, M. L. Stone, J. Schmidt, J. G. Thomas, Q. Ding, H.-C. Chang, M.-L. Tsai, J.-H. He and S. Jin, *Nat. Mater.*, 2015, **14**, 1245–1251.

33 C. M. A. Brett and A. M. O. Brett, *Electrochemistry: Principles, Methods, and Applications*, Oxford University Press, Oxford, 1993.

34 Z. Feng, C. Liang, W. Wu, Z. Wu, R. A. van Santen and C. Li, *J. Phys. Chem. B*, 2003, **107**, 13698–13702.

35 H. Li, Q. Zhang, C. C. R. Yap, B. K. Tay, T. H. T. Edwin, A. Olivier and D. Baillargeat, *Adv. Funct. Mater.*, 2012, **22**, 1385–1390.

36 J. Suh, T.-E. Park, D.-Y. Lin, D. Fu, J. Park, H. J. Jung, Y. Chen, C. Ko, C. Jang, Y. Sun, R. Sinclair, J. Chang, S. Tongay and J. Wu, *Nano Lett.*, 2014, **14**, 6976–6987.

37 D. Kiriya, M. Tosun, P. Zhao, J. S. Kang and A. Javey, *J. Am. Chem. Soc.*, 2014, **136**, 7853–7856.

38 Z. Xing, Q. Liu, A. M. Asiri and X. Sun, *Adv. Mater.*, 2014, **26**, 5702–5707.

39 L. Ji, M. D. McDaniel, S. Wang, A. B. Posadas, X. Li, H. Huang, J. C. Lee, A. A. Demkov, A. J. Bard, J. G. Ekerdt and E. T. Yu, *Nat. Nanotechnol.*, 2015, **10**, 84–90.

40 J. Kibsgaard and T. F. Jaramillo, *Angew. Chem., Int. Ed.*, 2014, **53**, 14433–14437.

41 A. J. Bard and L. R. Faulkner, *Electrochemical Methods: Fundamentals and Applications*, John Wiley & Sons, Inc., New York, 2001.

42 S. Hernández, D. Hidalgo, A. Sacco, A. Chiodoni, A. Lamberti, V. Cauda, E. Tresso and G. Saracco, *Phys. Chem. Chem. Phys.*, 2015, **17**, 7775–7786.

43 K. Ojha, S. Saha, H. Kolev, B. Kumar and A. K. Ganguli, *Electrochim. Acta*, 2016, **193**, 268–274.

44 D. M. Andoshe, S. Choi, Y.-S. Shim, S. H. Lee, Y. Kim, C. W. Moon, D. H. Kim, S. Y. Lee, T. Kim, H. K. Park, M. G. Lee, J.-M. Jeon, K. T. Nam, M. Kim, J. K. Kim, J. Oh and H. W. Jang, *J. Mater. Chem. A*, 2016, **4**, 9477–9485.

45 U. Sim, T.-Y. Yang, J. Moon, J. An, J. Hwang, J.-H. Seo, J. Lee, K. Y. Kim, J. Lee, S. Han, B. H. Hong and K. T. Nam, *Energy Environ. Sci.*, 2013, **6**, 3658–3664.

46 Q. Ding, F. Meng, C. R. English, M. Cabán-Acevedo, M. J. Shearer, D. Liang, A. S. Daniel, R. J. Hamers and S. Jin, *J. Am. Chem. Soc.*, 2014, **136**, 8504–8507.

47 Q. Ding, B. Song, P. Xu and S. Jin, *Chem*, 2016, **1**, 699–726.